

PARTICLE PHYSICS

Direct neutrino-mass measurement based on 259 days of KATRIN data

KATRIN Collaboration†, Max Aker¹, Dominic Batzler¹, Armen Beglarian², Jan Behrens¹, Justus Beisenkötter³, Matteo Biassoni⁴, Benedikt Bieringer³, Yanina Biondi¹, Fabian Block¹, Steffen Bobien⁵, Matthias Böttcher³, Beate Bornschein¹, Lutz Bornschein¹, Tom S. Caldwell^{6,7}, Marco Carminati^{8,9}, Auttakit Chatrabhuti¹⁰, Suren Chilingaryan², Byron A. Daniel¹¹, Karol Debowski¹², Martin Descher¹³, Deseada Díaz Barrero¹, Peter J. Doe^{14,15}, Otokar Dragoun¹⁶, Guido Drexlin¹³, Frank Edzards^{17,18}, Klaus Eitel¹, Enrico Ellinger¹², Ralph Engel^{1,13}, Sanshiro Enomoto^{14,15}, Arne Felden¹, Caroline Fengler¹, Carlo Fiorini^{8,9}, Joseph A. Formaggio¹⁹, Christian Forstner^{17,18}, Florian M. Fränkle¹, Kevin Gauda³, Andrew S. Gavin^{6,7}, Woosik Gil¹, Ferenc Glück¹, Steffen Grohmann²⁰, Robin Grösse¹, Rainer Gumbsch¹, Nathanael Gutknecht¹³, Volker Hannen³, Leonard Hasselmann¹, Norman Haußmann¹², Klaus Helbing¹², Hanna Henke¹, Svenja Heyns¹, Stephanie Hickford¹, Roman Hiller¹, David Hillesheimer¹, Dominic Hinz¹, Thomas Höhn¹, Anton Huber¹, Alexander Jansen¹, Christian Karl¹⁷, Jonas Kellerer¹, Khanchai Khosonthongkee²¹, Matthias Kleifges², Manuel Klein¹, Joshua Kohpeiß¹, Christoph Köhler^{17,18}, Leonard Köllenberger¹, Andreas Kopmann², Neven Kovac¹, Alojz Kovalik¹⁶, Holger Krause¹, Luisa La Cascio¹³, Thierry Lasserre²², Joscha Lauer¹, Thanh-Long Le¹, Ondřej Lebeda¹⁶, Bjoern Lehnert²³, Gen Li¹¹, Alexey Lokhov^{13*}, Moritz Machatschek¹, Martin Mark¹, Alexander Marsteller^{1,14,15}, Eric L. Martin^{6,7}, Christin Melzer¹, Susanne Mertens^{17,18,24}, Shailaja Mohanty¹, Jalal Mostafa², Klaus Müller¹, Andrea Nava^{4,25}, Holger Neumann⁵, Simon Niemes¹, Anthony Onillon^{17,18}, Diana S. Parno¹¹, Maura Pavan^{4,25}, Udomsilp Pinsook¹⁰, Alan W. P. Poon²³, Jose Manuel Lopez Poyato²⁶, Stefano Pozzi⁴, Florian Priester¹, Jan Ráliš¹⁶, Shivani Ramachandran¹², R. G. Hamish Robertson^{14,15}, Caroline Rodenbeck^{1,3}, Marco Rölli¹, Carsten Röttle¹, Milos Ryšavý¹⁶, Rudolf Sack¹, Alejandro Saenz²⁷, Richard Salomon³, Peter Schäfer¹, Magnus Schlösser¹, Klaus Schlösser¹, Lisa Schlüter^{18,23}, Sonja Schneidewind³, Ulrich Schnurr¹, Michael Schrank¹, Jannis Schürmann^{3,27}, Ann-Kathrin Schütz²³, Alessandro Schwemmer^{17,18}, Adrian Schwenck¹, Michal Šefčík¹⁶, Daniel Siegmann^{17,18}, Frank Simon², Felix Spanier²⁸, Daniela Spreng^{17,18}, Warintorn Sreethawong²¹, Markus Steidl¹, Jaroslav Štorek¹, Xaver Strbl^{17,18}, Michael Sturm¹, Narumon Suwonjandee¹⁰, Nicholas Tan Jerome², Helmut H. Telle²⁶, Larisa A. Thorne²⁹, Thomas Thümmler¹, Simon Tirolf¹, Nikita Titov³⁰, Igor Tkachev³⁰, Korbinian Urban^{17,18}, Kathrin Valerius¹, Drahoslav Vénos¹⁶, Christian Weinheimer³, Stefan Welte¹, Jürgen Wendel¹, Christoph Wiesinger^{17,18,24*}, John F. Wilkerson^{6,7}, Joachim Wolf¹³, Sascha Wüstling², Johanna Wydra¹, Weiran Xu¹⁹, Sergey Zadorozhny³⁰, Genrich Zeller¹

That neutrinos carry a nonvanishing rest mass is evidence of physics beyond the Standard Model of elementary particles. Their absolute mass holds relevance in fields from particle physics to cosmology. We report on the search for the effective electron antineutrino mass with the KATRIN experiment. KATRIN performs precision spectroscopy of the tritium β -decay close to the kinematic endpoint. On the basis of the first five measurement campaigns, we derived a best-fit value of $m_\nu^2 = -0.14^{+0.13}_{-0.15}$ eV², resulting in an upper limit of $m_\nu < 0.45$ eV at 90% confidence level. Stemming from 36 million electrons collected in 259 measurement days, a substantial reduction of the background level, and improved systematic uncertainties, this result tightens KATRIN's previous bound by a factor of almost two.

Neutrino flavor oscillations imply the existence of distinct neutrino mass states, ν_i , with mass values, m_i , and contradict the hypothesis of massless neutrinos in the Standard Model of elementary particles (1, 2). Although the squared splittings of these mass values have been measured with ever-increasing precision (3, 4), the absolute neutrino mass scale remains unknown. Neutrinos are at least six orders of magnitude lighter than other fermions, suggesting a new type of mass-generation mechanism that could involve heavy nonactive neutrinos (5–8).

Neutrinos interact as flavor states, ν_ℓ , where ℓ identifies the corresponding charged-lepton partner: the electron, e , the muon, μ , and the tau, τ (9, 10). Neutrino flavor oscillations identify these flavor states as superpositions of the

mass states. The Pontecorvo-Maki-Nakagawa-Sakata (PMNS) mixing matrix elements $U_{\ell i}$ encode the ν_i admixture of ν_ℓ (11, 12).

Neutrinos are the most abundant massive known particles in our universe. Their late transition from hot to cold matter leaves an imprint on the cosmic evolution and structure formation. The combination of several observational data sets, analyzed within the framework of standard cosmology, provides a stringent bound of 0.072 eV at 95% credible interval (CI) (13, 14) for the neutrino mass sum, $\sum m_i$ (15). This bound can be relaxed in the case of nonstandard physics [for example, (16–18)].

Neutrinos carry neither electric nor color charges. Hence, they may be Majorana particles—fermions that are their own antiparticles (19). This hypothesis is tested with experiments

searching for neutrinoless double- β -decay (20). Assuming mediation by light Majorana neutrinos, upper limits on the effective Majorana neutrino mass— $|\sum_i U_{ei}^2 m_i|$, the coherent sum of neutrino masses weighted by their squared electron neutrino contribution—were placed at 0.079 to 0.180 eV at 90% confidence level (CL) for ⁷⁶Ge (21), 0.070 to 0.240 eV at 90% CI for ¹³⁰Te (22), and 0.036 to 0.156 eV at 90% CL for ¹³⁶Xe (23, 24).

A direct way to assess the neutrino mass is provided by β -decay kinematics, in which the neutrino mass modifies the phase space for the emission of electrons with kinetic energy E . The shape distortion of the differential β -decay spectrum

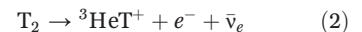
$$R_\beta(E; E_0, m_\nu^2) \propto (E_0 - E) \cdot \sqrt{(E_0 - E)^2 - m_\nu^2} \quad (1)$$

is maximal near the kinematic endpoint E_0 , which is defined as the maximal energy of the β -decay electrons assuming $m_\nu = 0$ (25). Because each neutrino mass state contributes individually with its own admixture but is typically not resolved, the squared effective electron antineutrino mass, $m_\nu^2 = \sum_i |U_{ei}|^2 m_i^2$, is probed with a precise measurement of the β -decay spectrum shape near the endpoint (26). Unlike the above-mentioned methods, this approach is independent of both the cosmological model and the neutrino nature.

The Karlsruhe Tritium Neutrino experiment (KATRIN) leads the direct neutrino mass exploration. On the basis of the first measurement campaign, long-standing bounds on the neutrino mass obtained by the previous Mainz and Troitsk experiments (27, 28) were improved by a factor of two (29). The addition of the second campaign resulted in the world's first subconstraint of $m_\nu < 0.8$ eV at 90% CL (30), which was based on 6 million electron events in the analysis region. In this work, we present the result of the first five measurement campaigns with 36 million electrons collected across 259 measurement days.

Experimental setup

KATRIN performs precision β spectroscopy close to the kinematic endpoint, $E_0 \approx 18.6$ keV, of molecular tritium decay



It combines a high-activity gaseous tritium source of up to 100 with a high-resolution spectrometer (31). The 70-m-long KATRIN beamline is illustrated in Fig. 1.

Tritium is continuously reprocessed by the Tritium Laboratory Karlsruhe (TLK), delivering a tritium throughput of up to 40 g/day with up to 99% isotopic purity to the KATRIN source (32). Starting at a magnetic field of $2.507 \text{ T} \pm 0.25\%$, the β -decay electrons are guided adiabatically

through the windowless source and the transport section, where the tritium is removed by means of differential and cryogenic pumping (33, 34). The upstream flux of electrons is terminated with a gold-plated rear wall. A voltage of $\mathcal{O}(100\text{ mV})$ is applied to the rear wall to control the source potential (31).

The spectrometer section consists of a pre-spectrometer followed by the 23-m-long, 10-m-wide main spectrometer, both of which use the magnetic adiabatic collimation with electrostatic filtering (MAC-E) principle (35, 36). The electron momenta, $\vec{p} = \vec{p}_\perp + \vec{p}_\parallel$, are aligned with the field lines of a magnetic field relaxing in strength, B , owing to the conservation of the electron orbital magnetic moment, $\mu \propto \frac{p_\perp^2}{B}$. In the main spectrometer, the magnetic field strength decreases to minimum values of 0.45 to 0.63 mT. The simultaneous application of a precisely known electrostatic retarding potential (37), U , allows only electrons of charge $q = -e$ and energy $E < qU$ to pass the so-called

analyzing plane, where maximal collimation and retardation coincide. With the maximal magnetic field in the beamline of $4.24\text{ T} \pm 0.1\%$, an acceptance of electrons emitted with a pitch angle of up to 51° and an excellent energy filter width of 2.0 to 2.8 eV for different parts of the flux are achieved. The integral flux of transmitted electrons is measured with the focal plane detector (FPD), a 148-pixel silicon-PIN-diode array, featuring a detection efficiency of about 95% (38).

KATRIN is monitored by more than 5700 sensors, recording numerous operational parameters such as the tritium purity, the temperatures of different beamline components, and the magnetic fields (31). Additionally, the beamline is equipped with several calibration sources. An angular-selective source of mono-energetic photoelectrons (electron gun) (39) is used to measure the gas density in the tritium source down to subpercent precision. The cocirculation of ^{83m}Kr with tritium and other carrier gases (40, 41) allows us to determine the electron starting potential within the source and the electromagnetic fields in the spectrometer.

Despite the high-activity tritium source, the signal count rate is less than one count per second (cps) at $qU \geq E_0 - 10\text{ eV}$, which puts stringent requirements on the acceptable background rate. External backgrounds caused by gamma radiation and cosmic-ray muons are mitigated by the magnetic shielding and the electric potential on the wire electrode system of the MAC-E spectrometers (31, 42, 43). The ^{219}Rn and ^{220}Rn decay backgrounds are successfully suppressed by liquid nitrogen-cooled copper baffles in the main-spectrometer pumping ducts (44, 45). Particles stored in a Penning trap between the two spectrometers generate another source of background. These accumulated particles are removed by

a conductive wire periodically clearing the trap volume (46). The background contribution of the detector system is suppressed by a region-of-interest (ROI) cut on the detected energy, a muon veto system, and postacceleration of the electrons (38).

The remaining background is dominated by neutral atoms in highly excited states, which are sputtered off the spectrometer's inner surface by the decays of residual ^{210}Pb and its daughter ^{210}Po . These atoms are distributed throughout the spectrometer volume. Their loosely bound electrons are easily released by blackbody radiation or by autoionization and are accelerated up to signal-electron energies toward the detector (47). A method to reduce this background is a reconfiguration of the electromagnetic fields in the main spectrometer, which results in a smaller collection volume for these background electrons. It comprises both a compression of the magnetic flux tube and a downstream shift of the analyzing plane, which is nominally situated in the center of the main spectrometer (48). This shifted-analyzing-plane (SAP) setting was implemented over the course of the new measurement campaigns (Table 1).

Measurement overview

KATRIN obtains the integral β spectrum by measuring the count rate at the FPD for a defined sequence of retarding-energy set points, qU_i , forming a β -spectrum scan. Each scan is typically composed of up to 40 set points in a range of $E_0 - 300\text{ eV} \leq qU_i \leq E_0 + 135\text{ eV}$. The neutrino mass analysis is limited to data points above $E_0 - 40\text{ eV}$. The spectrum points above the endpoint constrain the background rate. The data recorded below the endpoint, outside of the analysis range, is used for calibration and monitoring purposes. The total duration of a β -spectrum scan ranges from

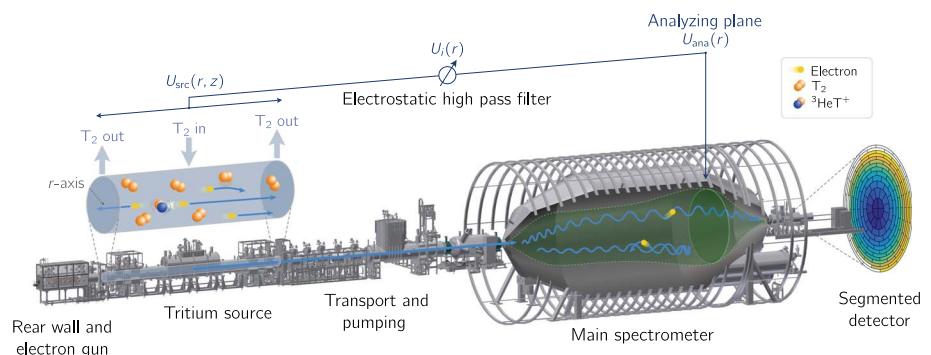


Fig. 1. The KATRIN beamline. Tritium gas is continuously injected into the source, where it decays, producing β -electrons. (Inset) The source volume, filled with a plasma of low-energy electrons and tritiated ions. The tritium gas is pumped out, purified, and recirculated, whereas the electrons are guided magnetically through the transport section into the spectrometer. Only electrons with sufficient energy to overcome the electrostatic potential in the analyzing plane are counted at the detector. The analyzing plane is shifted toward the detector for background reduction.

¹Institute for Astroparticle Physics (IAP), Karlsruhe Institute of Technology (KIT), Eggenstein-Leopoldshafen, Germany. ²Institute for Data Processing and Electronics (IPE), KIT, Eggenstein-Leopoldshafen, Germany. ³Institute for Nuclear Physics, University of Münster, Münster, Germany. ⁴Istituto Nazionale di Fisica Nucleare (INFN)–Sezione di Milano–Bicocca, Milano, Italy. ⁵Institute for Technical Physics (ITEP), KIT, Eggenstein-Leopoldshafen, Germany. ⁶Department of Physics and Astronomy, University of North Carolina, Chapel Hill, NC, USA. ⁷Triangle Universities Nuclear Laboratory, Durham, NC, USA. ⁸Politecnico di Milano, Dipartimento di Elettronica, Informazione e Bioingegneria, Milano, Italy. ⁹INFN–Sezione di Milano, Milano, Italy. ¹⁰Department of Physics, Faculty of Science, Chulalongkorn University, Bangkok, Thailand. ¹¹Department of Physics, Carnegie Mellon University, Pittsburgh, PA, USA. ¹²Department of Physics, Faculty of Mathematics and Natural Sciences, University of Wuppertal, Wuppertal, Germany. ¹³Institute of Experimental Particle Physics (ETP), KIT, Karlsruhe, Germany. ¹⁴Center for Experimental Nuclear Physics and Astrophysics, University of Washington, Seattle, WA, USA. ¹⁵Department of Physics, University of Washington, Seattle, WA, USA. ¹⁶Nuclear Physics Institute, Czech Academy of Sciences, Řež, Czech Republic. ¹⁷Technical University of Munich, TUM School of Natural Sciences, Physics Department, Garching, Germany. ¹⁸Max Planck Institute for Physics, Garching, Germany. ¹⁹Laboratory for Nuclear Science, Massachusetts Institute of Technology, Cambridge, MA, USA. ²⁰Institute for Technical Thermodynamics and Refrigeration, KIT, Karlsruhe, Germany. ²¹School of Physics and Center of Excellence in High Energy Physics and Astrophysics, Suranaree University of Technology, Nakhon Ratchasima, Thailand. ²²IRFU (DPH and APC), CEA, Université Paris-Saclay, Gif-sur-Yvette, France. ²³Nuclear Science Division, Lawrence Berkeley National Laboratory, Berkeley, CA, USA. ²⁴Max-Planck-Institut für Kernphysik, Heidelberg, Germany. ²⁵Dipartimento di Fisica, Università di Milano–Bicocca, Milano, Italy. ²⁶Departamento de Química Física Aplicada, Universidad Autónoma de Madrid, Madrid, Spain. ²⁷Institut für Physik, Humboldt-Universität zu Berlin, Berlin, Germany. ²⁸Institute for Theoretical Astrophysics, University of Heidelberg, Heidelberg, Germany. ²⁹Institut für Physik, Johannes-Gutenberg-Universität Mainz, Mainz, Germany. ³⁰Institute for Nuclear Research of Russian Academy of Sciences, Moscow, Russia. (Institutional status in the KATRIN collaboration has been suspended since 24 February 2022.)

*Corresponding author. Email: alexey.lokhov@kit.edu (A.L.); christoph.wiesinger@tum.de (C.W.)

†The collaboration consists of all listed authors. There are no additional authors or collaborators.

‡Present address: Department of Physics, Duke University, Durham, NC, USA.

Table 1. Key features of the measurement campaigns. The live time corresponds to the data used for analysis. The values are quoted for the number of active pixels in each measurement campaign and all the scan-steps above $E_0 - 40$ eV. The uncertainties of the pre-spectrometer voltage, source temperature, and background rate are below the precision of the reported significant digits.

	KNM1	KNM2	KNM3-SAP	KNM3-NAP	KNM4-NOM	KNM4-OPT	KNM5
Year	2019	2019	2020	2020	2020	2020	2021
Months	4 to 5	10 to 12	6 to 7	7	9 to 10	10 to 12	4 to 6
Measurement days	35	45	14	14	49	30	72
Analyzing plane	Nominal	Nominal	Shifted	Nominal	Shifted	Shifted	Shifted
Prespectrometer voltage (kV)	−10.5	−10.5	−10.5	−10.5	−10.5	−10.5/−0.1	−0.1
Scan-step duration	Nominal	Nominal	Nominal	Nominal	Nominal	Optimized	Optimized
Rear wall	Not cleaned	Not cleaned	Not cleaned	Not cleaned	Not cleaned	Not cleaned	Cleaned
Source temperature (K)	30	30	79	79	79	79	79
Background rate (cps)	0.29	0.22	0.12	0.22	0.13	0.13	0.14
Number of scans	274	361	114	116	320	150	422
Live time (hrs)	522	694	220	224	835	432	1226
Active pixels	117	117	126	126	126	126	126
Column density ($\times 10^{21} \text{ m}^{-2}$)	1.08 ± 0.01	4.20 ± 0.04	2.05 ± 0.02	3.70 ± 0.04	3.76 ± 0.04	3.76 ± 0.04	3.77 ± 0.03
Source activity (GBq)	23.9 ± 0.3	93.9 ± 0.9	45.8 ± 0.5	82.5 ± 0.8	83.9 ± 0.8	83.9 ± 0.8	84.2 ± 0.8
Number of counts ($\times 10^9$)	2.03	4.31	1.07	1.43	5.64	4.58	16.65

125 to 195 min for the different measurement campaigns, while the fraction of time spent at each scan step is optimized for neutrino mass sensitivity. The sequence of retarding-energy set points is increasing, decreasing, or randomly set.

Each KATRIN neutrino-mass (KNM) measurement campaign contains a few hundred β -spectrum scans. In this work, we present the first five campaigns, with the data taken between March 2019 and June 2021. Table 1 contains the relevant operational information. There were five key configuration changes.

(i) After an initial burn-in period, the tritium gas column density was raised from $\rho d = (1.08 \pm 0.01) \times 10^{21} \text{ m}^{-2}$ in KNM1 to $(4.20 \pm 0.04) \times 10^{21} \text{ m}^{-2}$ in KNM2 (30), corresponding to 84% of the design value. ρ is the average gas density, and $d = 10 \text{ m}$ is the length of the source.

(ii) Starting from KNM3, the background was reduced by a factor of two by using the shifted-analyzing-plane setting (48). We validated the feasibility of this configuration with β -spectrum scans in the shifted (KNM3-SAP) and nominal symmetrical (KNM3-NAP) analyzing-plane settings.

(iii) A powerful technique to characterize the electric-potential variations in the source with ^{83m}Kr conversion electrons was introduced after KNM3 (41). This method features a new cocirculation mode of ^{83m}Kr with tritium at a high column density of $\rho d = 3.8 \times 10^{21} \text{ m}^{-2}$. This column density, along with an increase of the source operating temperature from 30 to 79 K, was chosen as the nominal setting after KNM3-NAP to perform the β -spectrum scans under the same experimental conditions as those for the cocirculation systematics scans.

The relative concentration of ^{83m}Kr gas of 10^{-6} does not affect the gas properties.

(iv) The impact of the time-dependent accumulation of particles in the Penning trap between the two spectrometers was reduced during KNM4 by successively shortening the intervals before each clearing of the trap. As a first measure, the maximal intervals were shortened from 1080 to 600 s. Later, all scan steps were set to an equal duration of 100 s. Last, the effect was fully mitigated by reducing the prespectrometer potential and eliminating the Penning trap conditions. In addition, the relative time spent at each scan step was further optimized for a better neutrino mass sensitivity from the nominal (KNM4-NOM) to the optimized (KNM4-OPT) configuration.

(v) Over the course of the first four campaigns, the gold surface of the rear wall accumulated tritium, which produces additional β -decay electrons. The corresponding activity was proportional to an integral tritium flow of $2.9 \times 10^7 \text{ mbar} \cdot \text{s}$. Before the start of KNM5, the accumulated tritium was reduced by a factor of 10^3 through ozone cleaning of the rear wall (49).

Data analysis

In total, 1757 out of 1895 scans with 117 (in KNM1 and -2) and later 126 (in KNM3-SAP, 3-NAP, 4-NOM, 4-OPT, and 5) out of 148 pixels were selected for the analysis (50). This selection excludes scans in which the monitoring systems indicated instabilities in electromagnetic fields or source parameters, and pixels that were shadowed by structural material of the beamline. The total number of counts in the analysis range was 36 million, which includes

both signal electrons and background. Compared with the previous result reported in (30), the statistics improved by a factor of six.

The high reproducibility of the retarding-energy set points [with a standard deviation of $<10 \text{ mV}$ (37)] and the stability of the operational parameters allowed the combination of the β -spectrum scans within one campaign by summing the counts recorded at a given set point. Analogously, the statistically independent spectra recorded by different detector pixels were combined. For campaigns operated in the nominal-analyzing-plane configuration, the counts of all pixels were summed. For the shifted-analyzing-plane configuration, the pixels were grouped into 14 ring-like detector patches, to account for the electric-potential and magnetic-field variations in the analyzing plane. This data combination procedure facilitated the analysis while introducing negligible additional uncertainties that are below 0.001 eV^2 for the m_ν^2 parameter.

The expected rate $R_{\text{calc}}(qU_i)$ at each retarding-energy set point, qU_i , was derived from the theoretical tritium β -decay energy spectrum, $R(E; E_0, m_\nu^2)$, convolved with the experimental response function, $f_{\text{calc}}(E, qU_i)$

$$R_{\text{calc}}(qU_i) = A_s N_T \int_{qU_i}^{\infty} R_\beta(E; E_0, m_\nu^2) f_{\text{calc}}(E, qU_i) dE + R_{\text{bg}} \quad (3)$$

The theoretical β -decay spectrum was calculated with Fermi's golden rule (51). Molecular effects were encoded in the final-states distribution, which describes the probability to populate different molecular states by the decay of molecular

tritium and was obtained with ab initio calculations (52, 53). This effect was included in R_b .

The response function describes the transmission probability of electrons through the MAC-E filter and takes into account the energy losses caused by inelastic scattering on tritium molecules in the source. N_T depends on the number of tritium atoms in the source, the maximum acceptance angle of the MAC-E filter, and the detection efficiency. The normalization factor A_s , the background rate R_{bg} , the effective endpoint energy E_0 , and the squared neutrino mass m_ν^2 are free parameters of the model.

To take into account the different experimental conditions, each campaign was described with an individual model. Likewise, the spectra recorded by different detector patches were described by individual models. The parameter inference was performed by a combined maximum-likelihood fit to statistically independent data sets p , minimizing the sum of the negative logarithm of the likelihoods, $-2\log\mathcal{L} = -2\sum_p \log\mathcal{L}_p$. For the campaigns operated in the nominal-analyzing-plane configuration, we used the standard normal likelihood function, assuming a Gaussian distribution of the measured counts. For campaigns in the shifted analyzing plane configuration, where the subdivision of data into detector patches led to a 14-times-lower count rate, we used the Poisson likelihood function.

To include systematic uncertainties, we extended the likelihood function with pull terms of the form $(\vec{\eta} - \vec{\eta}_{\text{ext}})^T \Theta_{\text{cov}}^{-1} (\vec{\eta} - \vec{\eta}_{\text{ext}})$. This allowed the experimental parameters, $\vec{\eta}$, such as the magnetic fields and tritium column density, to vary according to the covariance matrix, Θ_{cov} , around our best external estimate, $\vec{\eta}_{\text{ext}}$, which is typically obtained from dedicated calibration measurements.

Owing to the high degree of data segmentation, resulting in a total of 1609 data points, each minimization step required $\mathcal{O}(10^3)$ computationally expensive evaluations of $R_{\text{calc}}(qU_i)$. To overcome this computational challenge, we used two methods: a highly optimized direct calculation of the model (51) and a fast model prediction with a neural network (54).

To eliminate experimenter's bias, the analysis was carried out by two independent teams applying a two-step approach. First, the full analysis was performed on simulated data sets that mimicked the recorded experimental conditions of each scan. Second, when analyzing the data we used a model-blinding scheme in which we altered the variance of the molecular final-states distribution by an unknown value, so that m_ν^2 acquires an unknown bias. The unmodified true final-states distribution was only used after the analysis procedure and input parameters had been fixed.

This step was performed twice. After unblinding, a mistake in the data combination of the KNM4 campaign was uncovered. The change

of the relative scan-step durations, in combination with a drift of the starting potential, requires this data set to be separated into two periods, KNM4-NOM and KNM4-OPT. Additionally, a thorough review of all analysis inputs was repeated. The following modifications were made: The model of the time-dependent background was changed to a nonlinear description, motivated by simulations and additional mea-

surements; the uncertainties of the energy loss function were reevaluated; and the energy-dependent angle of the monoenergetic photoelectron source was included in the column density evaluation. The change of the best-fit m_ν^2 value attributed to these modifications was small compared with the uncertainty, whereas the systematic uncertainties have increased. The details are provided in (55).

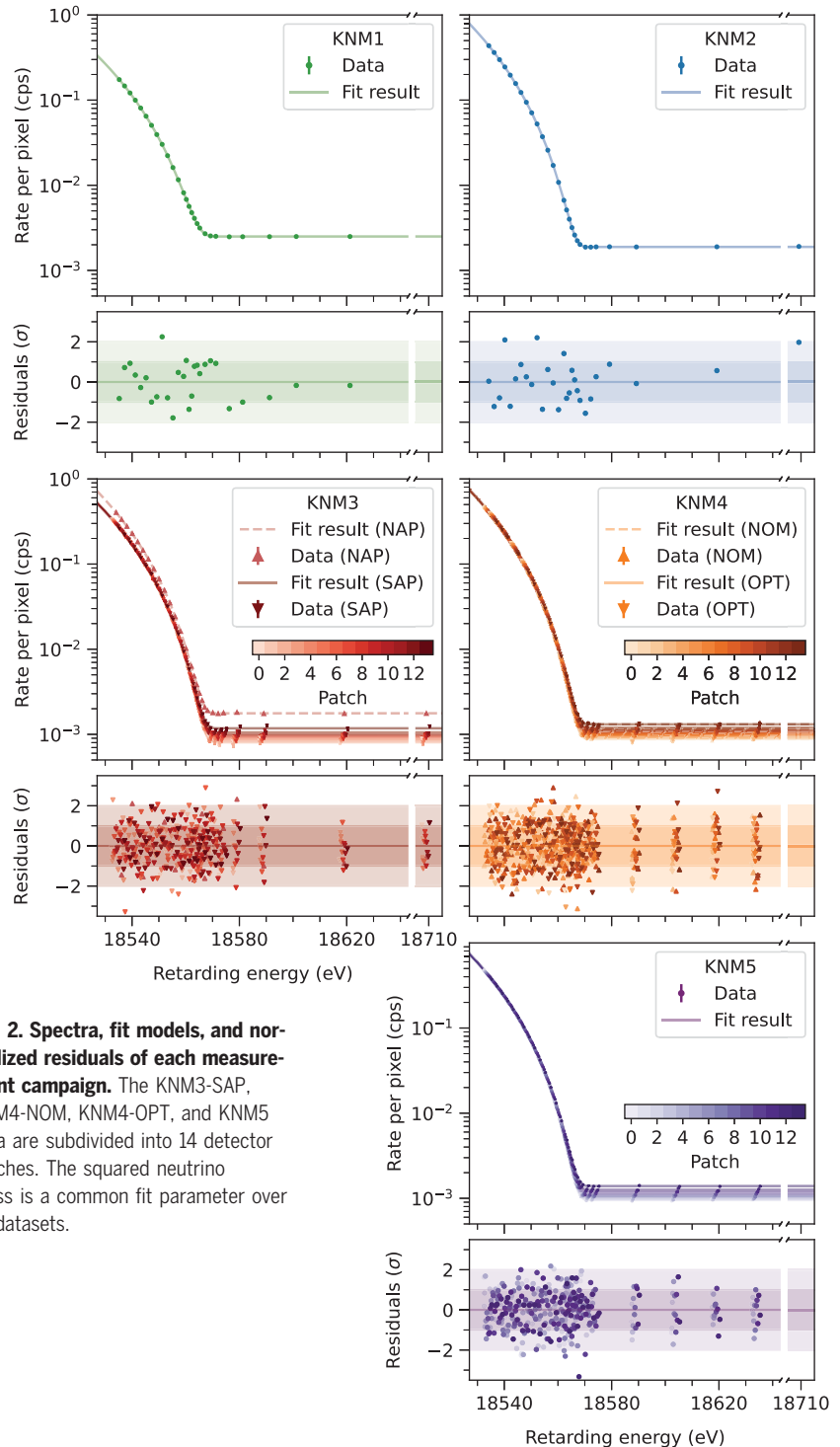


Fig. 2. Spectra, fit models, and normalized residuals of each measurement campaign. The KNM3-SAP, KNM4-NOM, KNM4-OPT, and KNM5 data are subdivided into 14 detector patches. The squared neutrino mass is a common fit parameter over all datasets.

Results

The simultaneous fit of the first five measurement campaigns yielded a squared neutrino mass of $m_\nu^2 = -0.14^{+0.13}_{-0.15} \text{ eV}^2$ with an excellent goodness of fit. The corresponding P value was 0.84. Negative m_ν^2 estimates stemming from statistical fluctuations were allowed by the spectrum model. Both analysis teams obtained the same result within 4% of the total m_ν^2 uncertainty. The spectra of each campaign and each detector patch are shown in Fig. 2. The total uncertainty was dominated by the statistical error, followed by the uncertainties of the column density, the energy-loss function, the time-dependent background rate, and the source-potential variations. The uncertainties are listed in Table 2.

On the basis of this best-fit result, we obtained an upper limit of $m_\nu < 0.45 \text{ eV}$ at 90% CL, using the Lokhov-Tkachov method (56). By construction, this upper limit equals the sensitivity of the experiment. This technique avoids shrinking upper limits for more negative values of m_ν^2 , which is characteristic for other methods, such as the Feldman-Cousins method (57). For completeness, the upper limit from the latter was $m_\nu < 0.31 \text{ eV}$ at 90% CL.

The effective endpoint, E_0 , is directly related to the Q value of the tritium β decay when taking into account the work function differences between the source, the rear wall, and the spectrometer as well as the recoil energy of the molecular ion, $E_{\text{rec}} = 1.72 \text{ eV}$ (58). The Q value for T_2 β decay measured in the campaign with the best source-potential stability, KNM4-NOM, was $(18575 \pm 0.3) \text{ eV}$. This agrees with our previously published results (29, 31) but is in slight tension with independent measurements of the atomic-mass difference with precision Penning traps (59).

Discussion and outlook

In this work, we report on the first five measurement campaigns of the KATRIN experiment, performed across 259 measurement days from April 2019 to June 2021. With six times the statistics corresponding to 36 million electrons, various improvements of the experimental setup, and better control of systematic effects, the KATRIN sensitivity to the effective electron antineutrino mass was improved by about a factor of two compared with the previous result (30). This improvement was based on implementing a spectrometer setting that reduced the background by a factor of two, improved calibration methods by using quasi-monoenergetic electrons from the photoelectron source and ^{83m}Kr , and a different systematic approach to assess the molecular final-states uncertainty. We obtained a best-fit value of $m_\nu^2 = -0.14^{+0.13}_{-0.15} \text{ eV}^2$, tightening the laboratory-based direct bound to $m_\nu < 0.45 \text{ eV}$ at 90% CL. The evolution of the KATRIN results is shown in Fig. 3.

KATRIN aims to reach 1000 measurement days by the end of 2025. This will correspond to about five times the statistics of the work presented here. On the basis of the current operational conditions, we expect to reach a final sensitivity of better than 0.3 eV at 90% CL. Moreover, new methods to further reduce

the background (60) and improve the sensitivity are under investigation. A new photoelectron source, installed in 2022 at the start of KNM7, allows detailed and high-statistics measurements of the column density and energy-loss function, which are the dominant systematic effects of the current analysis. The

Table 2. Breakdown of the uncertainties based on the Asimov data set. Each contribution in the last block of the table is smaller than 0.002 eV² and are therefore not propagated into the fit. Detailed information about the various effects is provided in (55).

Effect	68.3% CL uncertainty on m_ν^2 (eV ²)
Statistical uncertainty	0.108
Non-Poissonian background	0.015
Column density × inelastic cross section	0.052
Energy-loss function	0.034
Scan-step-duration-dependent background	0.027
Source-potential variations	0.022
qU -dependent background slope	0.007
Analyzing-plane magnetic field and potential	0.006
Source magnetic field	0.004
Maximum magnetic field	0.004
Rear-wall residual tritium background	0.004
Molecular final-state distribution	<0.002
Activity fluctuations	<0.002
Detector efficiency	<0.002
Retarding-potential stability and reproducibility	<0.002
Theoretical corrections	<0.002

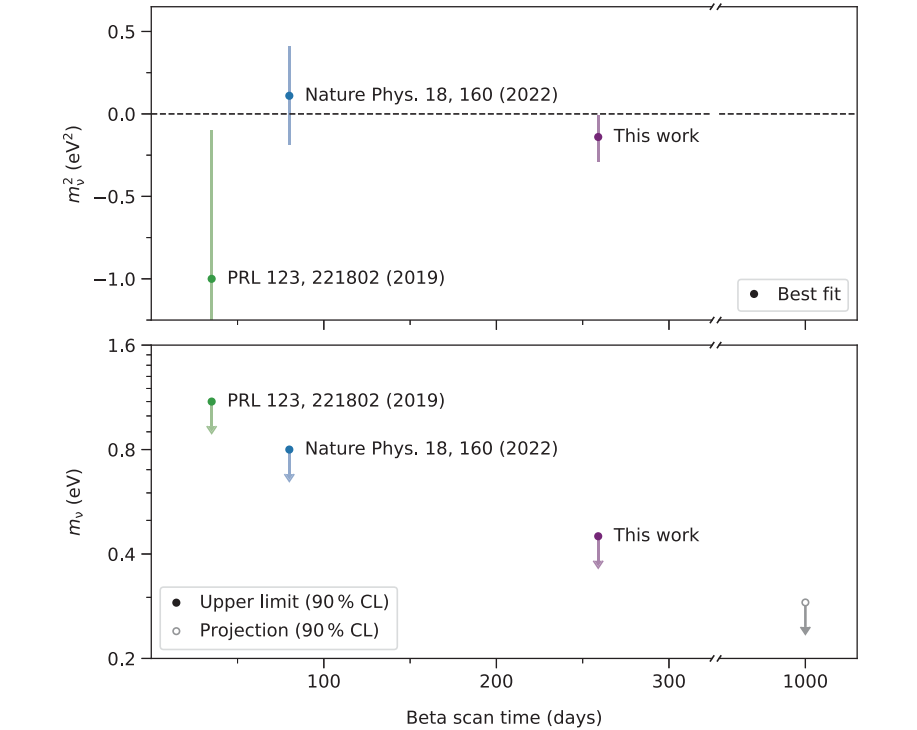


Fig. 3. Evolution of the KATRIN neutrino-mass results. The result obtained in this work (five measurement campaigns, purple) are compared with previous KATRIN results (first campaign, green, and combined first and second campaigns, blue).

scan-step-duration-dependent background has already been successfully mitigated over the course of the measurements presented here, and studies to reduce the uncertainty on the source-potential variations are ongoing.

Beyond the neutrino-mass investigation, the high-statistics and high-precision β -decay spectrum measured by KATRIN can be used to search for physics beyond the Standard Model of elementary particles, such as sterile neutrinos (67) and Lorentz-invariance violation (62), and to probe for the local neutrino overdensity (63).

REFERENCES AND NOTES

1. Y. Fukuda *et al.*, *Phys. Rev. Lett.* **81**, 1562–1567 (1998).
2. Q. R. Ahmad *et al.*, *Phys. Rev. Lett.* **89**, 011301 (2002).
3. I. Esteban, M. C. Gonzalez-Garcia, M. Maltoni, T. Schwetz, A. Zhou, *J. High Energy Phys.* **2020**, 178 (2020).
4. F. Capozzi *et al.*, *Phys. Rev. D* **104**, 083031 (2021).
5. P. Minkowski, *Phys. Lett. B* **67**, 421–428 (1977).
6. M. Gell-Mann, P. Ramond, R. Slansky, *Conf. Proc. C* **790927**, 315–321 (1979).
7. R. N. Mohapatra, G. Senjanovic, *Phys. Rev. Lett.* **44**, 912–915 (1980).
8. T. Yanagida, *Conf. Proc. C* **7902131**, 95 (1979).
9. G. Danby *et al.*, *Phys. Rev. Lett.* **9**, 36–44 (1962).
10. K. Kodama *et al.*, *Phys. Lett. B* **504**, 218–224 (2001).
11. Z. Maki, M. Nakagawa, S. Sakata, *Prog. Theor. Phys.* **28**, 870–880 (1962).
12. B. Pontecorvo, *Zh. Eksp. Teor. Fiz.* **53**, 1717 (1967).
13. N. Aghanim *et al.*, *Astron. Astrophys.* **641**, A6 (2020).
14. A. G. Adame *et al.*, *arXiv:2404.03002 [astro-ph.CO]* (2024).
15. In this paper, we use natural units, meaning $c = 1$.
16. Y. Farzan, S. Hannestad, *J. Cosmol. Astropart. Phys.* **02**, 058 (2016).
17. I. M. Oldengott, G. Barenboim, S. Kahlen, J. Salvado, D. J. Schwarz, *J. Cosmol. Astropart. Phys.* **04**, 049 (2019).
18. M. Escudero, J. Lopez-Pavon, N. Rijs, S. Sandner, *J. High Energy Phys.* **12**, 119 (2020).
19. E. Majorana, *Nuovo Cim.* **14**, 171–184 (1937).
20. J. Schechter, J. W. F. Valle, *Phys. Rev. D Part. Fields* **25**, 2951–2954 (1982).
21. M. Agostini *et al.*, *Phys. Rev. Lett.* **125**, 252502 (2020).
22. D. Q. Adams *et al.*, *arXiv:2404.04453 [nucl-ex]* (2024).
23. S. Abe *et al.*, *Phys. Rev. Lett.* **130**, 051801 (2023).
24. The ranges correspond to different nuclear structure calculations.
25. Similar considerations apply to electron-capture processes (64).
26. In this paper, we use the term neutrino mass for m_ν . Some sources use the symbol m_β .
27. C. Kraus *et al.*, *Eur. Phys. J. C* **40**, 447–468 (2005).
28. V. Aseev *et al.*, *Phys. Rev. D Part. Fields Gravit. Cosmol.* **84**, 112003 (2011).
29. M. Aker *et al.*, *Phys. Rev. Lett.* **123**, 221802 (2019).
30. M. Aker *et al.*, *Nat. Phys.* **18**, 160–166 (2022).
31. The KATRIN Collaboration *et al.*, *J. Instrum.* **16**, T08015 (2021).
32. D. Hillesheimer *et al.*, *Fus. Sci. Technol.* **80**, 465–471 (2024).
33. A. Marsteller *et al.*, *Vacuum* **184**, 109979 (2021).
34. C. Röttele *et al.*, *Vacuum* **208**, 111699 (2023).
35. V. M. Lobashev, P. E. Spivak, *Nucl. Instrum. Methods Phys. Res. A* **240**, 305–310 (1985).
36. A. Picard *et al.*, *Nucl. Instrum. Methods Phys. Res. B* **63**, 345–358 (1992).
37. C. Rodenbeck *et al.*, *J. Instrum.* **17**, P06003 (2022).
38. J. F. Amsbaugh *et al.*, *Nucl. Instrum. Methods Phys. Res. A* **778**, 40–60 (2015).
39. J. Behrens *et al.*, *Eur. Phys. J. C* **77**, 410 (2017).
40. J. Sentkerestiová *et al.*, *J. Instrum.* **13**, P04018 (2018).
41. A. Marsteller *et al.*, *J. Instrum.* **17**, P12010 (2022).
42. K. Altenmüller *et al.*, *Astropart. Phys.* **108**, 40–49 (2019).
43. K. Altenmüller *et al.*, *Eur. Phys. J. C* **79**, 807 (2019).
44. N. Wandkowsky *et al.*, *New J. Phys.* **15**, 083040 (2013).
45. S. Görhardt *et al.*, *J. Instrum.* **13**, T10004 (2018).
46. M. Aker *et al.*, *Eur. Phys. J. C* **80**, 821 (2020).
47. F. Fränkle *et al.*, *Astropart. Phys.* **138**, 102686 (2022).
48. A. Lokhov *et al.*, *Eur. Phys. J. C* **82**, 258 (2022).
49. M. Aker *et al.*, *Fus. Sci. Technol.* **80**, 303–310 (2024).
50. Nine pixels were recovered after the exchange of the detector wafer.
51. M. Kleesiek *et al.*, *Eur. Phys. J. C* **79**, 204 (2019).
52. A. Saenz, S. Jonsell, P. Froelich, *Phys. Rev. Lett.* **84**, 242–245 (2000).
53. N. Doss, J. Tennyson, A. Saenz, S. Jonsell, *Phys. Rev. C Nucl. Phys.* **73**, 025502 (2006).
54. C. Karl, P. Eller, S. Mertens, *Eur. Phys. J. C* **82**, 439 (2022).
55. Materials and methods are available as supplementary materials.
56. A. V. Lokhov, F. V. Tkachov, *Phys. Part. Nucl.* **46**, 347–365 (2015).
57. G. J. Feldman, R. D. Cousins, *Phys. Rev. D Part. Fields* **57**, 3873–3889 (1998).
58. E. W. Otten, C. Weinheimer, *Rep. Prog. Phys.* **71**, 086201 (2008).
59. M. Medina Restrepo, E. G. Myers, *Phys. Rev. Lett.* **131**, 243002 (2023).
60. K. Gauda *et al.*, *Eur. Phys. J. C* **82**, 922 (2022).
61. M. Aker *et al.*, *Phys. Rev. D* **105**, 072004 (2022).
62. M. Aker *et al.*, *Phys. Rev. D* **107**, 082005 (2023).
63. M. Aker *et al.*, *Phys. Rev. Lett.* **129**, 011806 (2022).
64. L. Gastaldo, *J. Low Temp. Phys.* **209**, 804–814 (2022).
65. KATRIN collaboration, Data set for Direct neutrino-mass measurement based on 259 days of KATRIN data. Zenodo (2024); <https://doi.org/10.5281/zenodo.13644900>.

ACKNOWLEDGMENTS

Funding: We acknowledge the support of the Helmholtz Association (HGF), Ministry for Education and Research BMBF (05A23PMA, 05A23PX2, 05A23VK2, and 05A23WO6), the doctoral school KSETA at KIT, Helmholtz Initiative and Networking Fund (grant agreement W2/W3-118), Max Planck Research Group (MaxPlanck@TUM), and Deutsche Forschungsgemeinschaft (DFG) (GRK 2149 and SFB-1258 and under Germany's Excellence Strategy EXC 2094–390783311) in Germany; the Ministry of Education, Youth, and Sport (CANAM-LM2015056, LTT19005) in the Czech Republic; Istituto Nazionale di Fisica Nucleare (INFN) in Italy; the National Science, Research, and Innovation Fund through the Program Management Unit for Human Resources & Institutional Development, Research and Innovation (grant B37G660014) in Thailand; and the US Department of Energy through awards DE-FG02-97ER41020, DE-FG02-94ER40818, DE-SC0004036, DE-FG02-97ER41033, DE-FG02-97ER41041, DE-SC0011091, and DE-SC0019304 and the Federal Prime Agreement DE-AC02-05CH11231 in the United States. This project has received funding from the European Research Council (ERC) under the European Union Horizon 2020 research and innovation program (grant agreement 852845). We thank the computing cluster support at the Institute for Astroparticle Physics at Karlsruhe Institute of Technology, Max Planck Computing and Data Facility (MPCDF), and the National Energy Research Scientific Computing Center (NERSC) at Lawrence Berkeley National Laboratory. **Author contributions:** All authors contributed to various aspects of the experiment, including the construction and operation, the data acquisition and analysis, the review of the analysis, and the approval of the manuscript. **Competing interests:** The authors declare no competing interests. **Data and materials availability:** The data and analysis inputs have been deposited at Zenodo (65). **License information:** Copyright © 2025 the authors, some rights reserved; exclusive licensee American Association for the Advancement of Science. No claim to original US government works. <https://www.science.org/about/science-licenses-journal-article-reuse>

SUPPLEMENTARY MATERIALS

science.org/doi/10.1126/science.adq9592
Materials and Methods
Supplementary Text
Figs. S1 to S17
References (66–86)

Submitted 10 June 2024; accepted 15 February 2025
10.1126/science.adq9592